

A microfluidic method and custom model for continuous, non-intrusive biofilm viscosity measurements under different nutrient conditions

J. Greener,^{1,a)} M. Parvinzadeh Gashti,¹ A. Eslami,² M. P. Zarabadi,¹ and S. M. Taghavi^{2,a)}

¹Department of Chemistry, Université Laval, 1045 Ave. de la Médecine, Québec, Québec G1V 0A6, Canada

²Department of Chemical Engineering, Université Laval, Québec, Québec G1V 0A6, Canada

(Received 9 July 2016; accepted 9 November 2016; published online 18 November 2016)

Straight, low-aspect ratio micro flow cells are used to support biofilm attachment and preferential accumulation at the short side-wall, which progressively reduces the effective channel width. The biofilm shifts downstream at measurable velocities under the imposed force from the constant laminar co-flowing nutrient stream. The dynamic behaviour of the biofilm viscosity is modeled semi-analytically, based on experimental measurements of biofilm dimensions and velocity as inputs. The technique advances the study of biofilm mechanical properties by strongly limiting biases related to non-Newtonian biofilm properties (e.g., shear dependent viscosity) with excellent time resolution. To demonstrate the proof of principle, young *Pseudomonas sp.* biofilms were analyzed under different nutrient concentrations and constant micro-flow conditions. The striking results show that large initial differences in biofilm viscosities grown under different nutrient concentrations become nearly identical in less than one day, followed by a continuous thickening process. The technique verifies that in 50 h from inoculation to early maturation stages, biofilm viscosity could grow by over 2 orders of magnitude. The approach opens the way for detailed studies of mechanical properties under a wide variety of physiochemical conditions, such as ionic strength, temperature, and shear stress. Published by AIP Publishing. [<http://dx.doi.org/10.1063/1.4968522>]

I. INTRODUCTION

Bacterial biofilms are heterogeneous viscoelastic materials, comprised of living bacteria enclosed within an extracellular polymeric matrix (EPM) of polysaccharides, DNA, and proteins. Their mechanical properties are complex and specially adapted to support survival, with a primary function to prevent detachment from a surface under shear flow conditions.^{4,27,33,40,43} The biofilm viscosity is an important property from the perspective of biofilm spreading (contamination) across surfaces,⁸ streamer formations,^{9,26,46} and biofilm cohesivity.¹⁰ Biofilm viscosity has also been noted to affect bacteriophage penetration through *Pseudomonas aeruginosa*. This is interesting because at the same time planktonic cell proliferation from *pseudomonas sp.* biofilms was shown to be nearly uniform under applied shear stresses in the range of 9.4 mPa–320 mPa, which almost certainly has an effect on the biofilm viscosity due to their non-Newtonian character.^{3,15} In addition to shear response, the complexity of biofilm viscosity can be traced to passive response to other environmental conditions, for example, in most cases, by thickening or thinning due to the presence of dissolved ionic species and thinning with increases to temperature.^{5,7,34,50} However, living biofilms are not only predicted to have

^{a)}Authors to whom correspondence should be addressed. Electronic addresses: Jesse.Greener@chm.ulaval.ca and Seyed-Mohammad.Taghavi@gch.ulaval.ca

different mechanical properties due to the mere physical presence of bacteria,¹ they also respond actively to their environment. Therefore, it is difficult to generalize how biofilms respond to their environments. For example, shear thinning has been reported for some strains such as *Streptococcus mutans* and *Chlorella vulgaris*^{7,54,57} and shear thickening in *P. aeruginosa*.¹⁹ Reported mechanical responses to different ions have also been varied.^{20,23,36} Moreover, living biofilms demonstrate intriguing time-dependent behaviour. For example, temporary increases to shear stress can be elastically absorbed by biofilms, but under long-term application, viscous flow becomes dominant as a mechanism to dissipate internal stresses.^{45,48} The characteristic time for this transition, the elastic relaxation time, is 18 min, which is assumed to be the result of the phenotypic changes to the bacteria.^{41,48,53}

Often elasticity is the focus of rheological studies of biofilms, with viscosity being produced as a by-product. For example, parallel plate rheometers³⁶ or analysis of stress-strain curves produced using time-limited changes to shear forces by cycling nutrient flow rates in growth cells.^{11,19,45,51,52} However, changes to imposed shear can induce measurement biases in viscosity for non-Newtonian biofilms. Moreover, since the time-scale of most laboratory growth experiments is longer than the elastic relaxation time quoted above, biofilms exhibit viscous liquid properties. This is particularly true for growth in microfluidic flow cells, which are becoming popular due to controlled laminar flow, eliminating chaotic fluctuations to shear.^{16,18,30,35} Despite being technically demanding, microrheology is a promising approach to obtain biofilm mechanical properties without inducing viscosity biases.^{7,8,44} However, until now no correlated fluctuation measurements have been undertaken, to ensure that the long-range properties are being measured,²⁴ which could help resolve the discrepancies in microrheology results.⁴ Most recently, a semi-empirical approach using a two-layer model of biofilms growing in microchannels has been demonstrated as a method to monitor time-varying viscosity. The technique was applied to follow biofilm development in time under different ionic strengths but required an estimation of biofilm height based on indirect measurements and a calibration method using transmission microscopy.³⁵

In this work, a measurement technique was devised which is based on continuous tracking of biofilm movement under slow, unchanging laminar flow. Measurements, therefore, could be made with excellent time resolution. With the aid of a new semi-analytical model, optical microscope measurements are interpreted to reveal viscosity. This was achieved by the development of a novel three-layer flow model in a rectangular cross-section microchannel with relevant boundary conditions. This approach contributes a new focus on viscosity properties to the growing body of work using fluid mechanics modeling methods for biofilms, such as thin-film asymptotic model to describe biofilm growth,^{12,13,56} mass transfer,³⁹ differential-discrete mathematical modelling of structure,³⁸ and others.⁵⁵ The approach opens the way for less intrusive, time-resolved studies of the effect of a range of physiochemical effects on biofilm mechanical properties, such as ionic strength.^{23,35}

The development of the rest of the paper is as follows. Section II explains our experimental setup. Section III discusses experimental observations. The details of our model are presented in Section IV. These include the geometry of the problem, the assumptions, the governing equations, the boundary conditions, the flux functions obtained, and the solution procedure. The results of the model are presented and discussed in Section V. Sections VI and VII conclude the paper with a discussion and summary.

II. EXPERIMENTAL SETUP

A transparent straight-channel microfluidic flow cell was fabricated with height, width, and length being $\hat{e} = 400$ (μm),³¹ $\hat{H} = 2000$ (μm), and $\hat{L} = 25$ (mm), respectively. The dimensions were chosen based on literature reports of biofilm accumulation at the microchannel side wall for channels with similar aspect ratios.¹⁷ Fabrication was accomplished by casting polydimethylsiloxane (PDMS) against a template mould (FlowJEM, Canada), which consisted of a photoresist (SU8-3000, Microchem) patterned on a silicon wafer support. The microchannel features in the PDMS were irreversibly sealed by a microscope coverslip (Fisher Scientific, USA)

via air plasma activation (PCD-001 Harrick Plasma, Ithaca, NY, USA). No channel sagging or collapse was observed in the sealed bonded channels (Fig. 1). We also note that while glass-PDMS devices are common for microfluidic studies of cells and biofilms, the heterogeneous surface environment of our channels should be acknowledged. Generally, it is known that a molecular conditioning layer can adsorb to the channel walls, rendering the surface chemistry similar⁴² even for initially heterogeneous environments. In addition, it is accepted that PDMS allows the easy exchange of small gas molecules between the microchannel contents and the ambient environment.²⁹ The combination of a slow flow rate (enabling longer time for gas exchange) and a high surface area to volume ratio of the low aspect channels was assumed to provide adequate O₂ concentrations for biofilm growth. Liquid delivery to the device was driven by a syringe pump (Harvard, PhD 2000) holding 60 (ml) polypropylene syringes (BD, USA), connected to perfluoroalkoxy (PFA) tubing (U-1148, IDEX, WA, USA). The nutrient solution consisted of diluted Luria-Bertani (PFA) medium, which consisted of 0.05 (wt. %) yeast extract and either 0.02 (wt. %) or 0.1 (wt. %) tryptone (Sigma-Aldrich, USA), 0.1 (wt. %) NaCl (Caledon Laboratories Ltd., Canada). Sterile distilled water was used in all cases. This formulation was between 10 and 50 times lower concentration of typical LB medium, to prevent catastrophic sloughing, which is known to happen for high nutrient concentrations.²¹ Biofilm-forming bacteria were *Pseudomonas* sp. CT07, which are considered equivalent to *Pseudomonas fluorescens* CT07,⁵⁸ were cultured at 30 (°C) for 3 days in an LB nutrient Petri dish via streaking. The bacteria were scraped from the surface and suspended in 3 (ml) of the nutrient medium. The tube was incubated overnight on an orbital shaker (300 (rpm)) at 30 (°C). Before inoculation of the microfluidic device, the tube, connectors, and microfluidic channel were all disinfected by first flowing 70% ethanol for 2 (h) at 1 (ml/h), followed by a 2 (ml/h) flow of sterilized distilled water for 1 (h). Inoculation was achieved by flowing bacteria pre-culture into the channels for 30 (min) at 0.1 (ml/h). After this, the inoculant flow was exchanged with a flow of the preprepared modified LB medium with a fixed volumetric flow rate of $\dot{Q}_2 = 0.1$ (ml/h), which corresponded to a velocity of $\hat{V}_0 = 125$ (mm/h) in the empty microchannel. At this flow rate, the dilution rate (reciprocal of residence time) was 10 (h⁻¹). As this was faster than the planktonic doubling rate in the bulk phase (<1 (h⁻¹)), we conclude that all changes to optical density (OD) were from the accumulated biofilm at the channel walls.² In order to minimize the thermal effect on bacterial metabolism or biofilm mechanical properties, the room temperature was set at 24.5 (°C). A local probe attached to the device verified that temperature stayed constant within 24.5 ± 0.50 (°C) during the experiments. Once the experiments started, no changes to volumetric flow rates or other experimental conditions were made.

Characterization through the transparent microfluidic channel was accomplished in the transmission mode, using an inverted microscope (IX-73, Olympus, Canada), with 2× objective

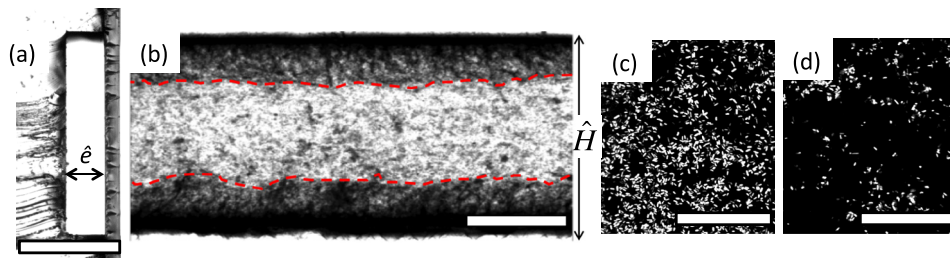


FIG. 1. (a) A cross-section of the microchannel bonded to a glass slide in the $\hat{x} - \hat{z}$ plane. The channel height is \hat{e} . (b) Biofilm layers growing at the sides of the microchannel at $t = 120$ (h) grown under 0.1 (ml/h) flow of a 0.1 (wt. %) tryptone LB nutrient solution. The red dashed line shows the approximate position of the visible biofilm edge. Subfigures (a) and (b) are oriented to have the same direction of their widths. \hat{H} is the microchannel width (2 (mm)) for images in (a) and (b). Flow was from left to right. Some contrast enhancement was applied to (b) to better visualize the wall adhered biofilm. The scale bars in (a) and (b) are both 1 (mm). Fluorescent images at $t = 70$ (h) showing individual green fluorescent protein (GFP) bacteria close to the vertical side wall (c) and close to the channel middle (d). Images were acquired with 60× oil immersion lens at a vertical distance of about 20 (μ m) from the glass surface, which was determined when the centre-located biofilm began to reduce in the number of bacteria, demonstrating its lower height. Scale bars in (c) and (d) are 50 (μ m).

(numerical aperture 0.06) and condenser with numerical aperture (0.9). A digital camera was used to collect 5 megapixel, 8-bit monochrome images, with exposure time, illumination intensity, and gain set by the controlling software (Image ProPlus 7.0, Media Cybernetics, USA). Time-lapse videos were created from the acquisition of micrographs every 30 min for 120 (h). Image analysis was conducted using the Fiji bundle for ImageJ.⁴⁷ Quantitative measurements of biofilm optical density (OD) were from pixel intensities using the first image in the time lapse movie series as a background. Image analysis of biofilm motion was accomplished using a particle tracking algorithm.²⁸ Here, we tracked identifiable portions of the biofilm in the $(\hat{x} - \hat{y})$ plane as they moved under the force of the flowing nutrient solution. An average time-dependent velocity was extracted from the entire dataset using the relation in the following equation:

$$\hat{v}_{\hat{t}} = \frac{\sum_i^N \frac{\hat{d}_{net,i}}{N}}{\Delta \hat{t}}, \quad (1)$$

where $\hat{v}_{\hat{t}}$ was the average velocity at time \hat{t} , i was a unique index value for each of the N tracked biofilm segments (typically $30 < N < 50$), $\hat{d}_{net,i}$ was their measured down-stream distance travelled between images, and $\Delta \hat{t}$ was the time interval between images (0.5 (h)).

III. EXPERIMENTAL RESULTS

Side-wall adhering biofilms were grown in microchannels under two different nutrient concentrations (0.02 (wt. %) and 0.1 (wt. %)) flowing at $\hat{Q}_2 = 0.1$ (ml/h). Nutrient flow rates at $\hat{Q}_2 = 0.2$ (ml/h) or higher did not produce side-wall adhered biofilms, likely due to unfavourable hydrodynamic conditions. As an example, the biofilm grown in 0.1 (wt. %) and $\hat{Q}_2 = 0.1$ (ml/h) could be seen accumulating at the side walls starting around 64 (h), after which its width continued to increase until about 80 (h) and remained constant during the entire measurement (Fig. 1). These trends are shown in Fig. 2 along with the change in width for the 0.02 (wt. %) sample, which increased more-or-less linearly for the entire observation time.

In this work, we assume that the biofilm occupies the entire vertical space between the bottom and top walls in the optically dense regions near the side walls (see Fig. 3) as has been observed in previous work and which is confirmed by the observation of flowing debris deviating from their flow trajectory to avoid certain local protrusions from the average biofilm/liquid interface.¹⁷ This resulted in a constriction in the channel dimensions, which in turn increased the flow velocity and shear force against the biofilm. As we mention in Section VI, however, the change in shear values due to moderate constrictions is very low. The instantaneous velocity of biofilm segments was obtained by tracking after wall accumulation started which yielded an average time varying biofilm flow velocity. This was conducted separately at each wall in order to account for possible differences in biofilm thickness. Next, a mathematical model was developed to convert the biofilm velocities and their transverse width to viscosities.

Figs. 2(a) and 2(b) show our experimental measurements. Fig. 2(a) depicts the variation of the width of the biofilm layer (\hat{h}) versus time (\hat{t}). Width measurements were performed after the accumulation of the biofilm at the microchannel wall for $\hat{t} \geq 64$ (h). The width of the biofilm layer increased with time. Fig. 2(b) shows the experimental value of the average speed of the biofilm layer.

IV. MATHEMATICAL MODEL

In this section, we develop a mathematical model to predict the biofilm viscosity. In the development of the model, we were inspired by a number of papers using two-layer fluid flows in rectangular ducts in different contexts.^{6,14,25} In terms of the mathematics, we extend these models to three-layer fluid flows. As well, and perhaps more importantly, we employ such methods to extract specific variables of the flow that can be effectively used for biofilm growth

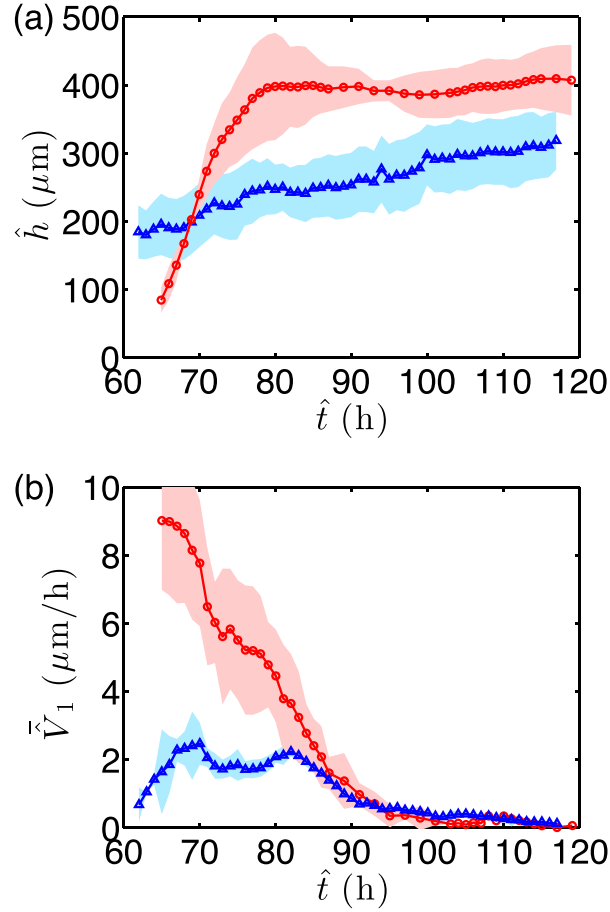


FIG. 2. (a) Width of the biofilm layer (\hat{h}) versus time (\hat{t}) from the beginning of the experiment. (b) The biofilm layer average speed (\hat{V}_1) versus time (\hat{t}) measured using our experiments. In each subfigure, two different nutrient concentrations are shown: 0.02 (wt. %) (blue triangles) and 0.1 (wt. %) (red circles). Shaded error bands were determined by standard deviation in measurement values at each time.

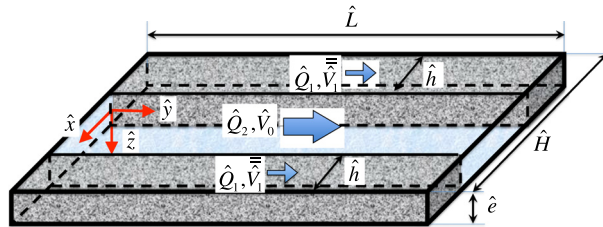


FIG. 3. The schematic view of the two-phase flow system and the relevant geometries. See Table I for units, relations, and values. The flow is symmetric with respect to the center of the channel. Biofilm layers are formed at channel side walls and grow with time. Each biofilm layer has a width of \hat{h} , which is the average value measured experimentally. Nutrient solution flow (large blue arrow) with volumetric flow rate \hat{Q}_2 and a mean imposed velocity $\hat{V}_0 = \hat{Q}_2 / \hat{A}$ (where \hat{A} is the channel cross section area) is from left to right. The resulting biofilm flow rate \hat{Q}_1 and mean velocity \hat{V}_1 are in the same direction (small blue arrow). Directionality of \hat{x} , \hat{y} , \hat{z} is defined with red arrows.

applications. Table I shows the dimensional and dimensionless parameters used in our experiments and model.

As time increases, we consider the formation of the biofilm along the vertical side-walls of the microchannel, whose width (\hat{h}) grows with time (\hat{t}), while its height remains equal to that of the microchannel (\hat{e}) at all times (Fig. 3). Under the pressure gradient $\hat{f} = -\frac{\partial \hat{p}}{\partial \hat{y}}$, there is an

TABLE I. Dimensional and dimensionless parameters used in our experiments and model.

| Variable symbol | Name | SI units | Value ranges | Scaled with | Unitless version |
|-------------------------------|---|-------------------|---|-------------------------------------|-------------------|
| \hat{h} | Biofilm width | m | $0\text{--}10^{-3}$ | \hat{e} | h |
| \hat{L} | Channel length | m | 25×10^{-3} | \hat{e} | L |
| \hat{H} | Channel width | m | 2×10^{-3} | \hat{e} | H |
| \hat{e} | Channel height | m | 4×10^{-4} | \hat{e} | 1 |
| \hat{A} | Channel cross section | m ² | 8×10^{-7} | \hat{e}^2 | A |
| $\hat{\mu}_2$ | Solution viscosity | Pa s | 10^{-3} | $\hat{\mu}_2$ | 1 |
| \hat{t} | Time | s | $0\text{--}432 \times 10^3$ | \hat{e}/\hat{V}_0 | T |
| $\hat{\bar{V}}_1$ | Biofilm flow velocity averaged over \hat{x} and \hat{z} | m/s | $0\text{--}2.8 \times 10^{-9}$ | \hat{V}_0 | $\bar{\bar{V}}_1$ |
| \hat{V}_0 | Solution mean imposed flow velocity | m/s | 3.47×10^{-5} | \hat{V}_0 | 1 |
| \hat{Q}_2 | Solution flow rate | m ³ /s | 2.78×10^{-11} | $\hat{V}_0 \hat{e}^2$ | Q_2 |
| $(\hat{x}, \hat{y}, \hat{z})$ | Cartesian coordinates | m | $(-1 \text{ to } 1, 0 \text{ to } 25, -0.2 \text{ to } 0.2) \times 10^{-3}$ | \hat{e} | (x, y, z) |
| \hat{p} | Pressure | N/m ² | Delivered by the model | $\hat{\mu}_2 \hat{V}_0 / \hat{e}$ | p |
| \hat{f} | Pressure gradient | N/m ³ | Delivered by the model | $\hat{\mu}_2 \hat{V}_0 / \hat{e}^2$ | f |
| $\hat{V}_1(\hat{x}, \hat{z})$ | Biofilm flow velocity | m/s | Delivered by the model | \hat{V}_0 | $V_1(x, z)$ |
| $\hat{V}_2(\hat{x}, \hat{z})$ | Solution flow velocity | m/s | Delivered by the model | \hat{V}_0 | $V_2(x, z)$ |
| $\hat{\bar{V}}_1(\hat{x})$ | Biofilm flow velocity averaged over \hat{z} | m/s | Delivered by the model | \hat{V}_0 | $\bar{V}_1(x)$ |
| \hat{Q}_1 | Biofilm flow rate | m ³ /s | Delivered by the model | $\hat{V}_0 \hat{e}^2$ | Q_1 |
| $\hat{\mu}_1$ | Biofilm viscosity | Pa s | Delivered by the model | $\hat{\mu}_2$ | m |

imposed flow of the solution (containing nutrients) into the microchannel with a mean speed of $\hat{V}_0 = \hat{Q}_2 / \hat{A}$, where \hat{Q}_2 is the imposed flow rate of the solution and \hat{A} is the cross sectional area of the microchannel. At each moment, we assume that the width of the biofilm is uniform along the microchannel and that the length of the biofilm layer is sufficiently long in the \hat{y} direction. The former assumption implies that the interfacial deformations, promoted by the flow profile in \hat{x} , relax faster than the gradient in \hat{y} .²⁵ We also assume that the interface between the two fluids is completely flat and we position the center of our Cartesian coordinates at the middle of the interface (i.e., at $\hat{e}/2$ with respect to the upper/lower walls). We neglect surface tension and we also assume that the interface between the two phases remains sharp. As Fig. 3 shows, the assumed configuration resembles a classical multi-layer fluid flow in a restricted geometry.

We consider a stationary, fully developed, parallel (purely viscous) flow of the two fluids involved: fluid 2 (the solution) and fluid 1 (the biofilm). Although biofilms are known to exhibit non-Newtonian properties,⁴⁸ for simplicity we assume the fluids involved to be both Newtonian. This assumption may be justified by considering that we are interested in longer time dynamics of the flow, which are beyond the relaxation time of the biofilm. As well, the imposed shear stresses are very low in our experiments, which may not induce a non-Newtonian response. Although the model that we develop here is rather general and it can be used for viscosity ratios both smaller and larger than 1, it is known that the biofilm normally has a larger viscosity compared to that of the solution. Fluid 2 moves downstream under the effect of the pressure gradient \hat{f} (assumed to be the same for the two fluids), while slowly dragging fluid 1 behind it. Using measurements of nutrient solution viscosity (supplementary material), we took the viscosity of fluid 2 to be constant with time and to be equal to that of water, i.e., $\hat{\mu}_2 = 1$ (mPa s). The densities of the fluids are assumed to be equal.

Using the assumptions mentioned, the Navier-Stokes equations are simplified and the problem reduces to finding the solution of Poisson equation

$$\nabla^2 \hat{V}_i(\hat{x}, \hat{z}) = -\hat{f} / \hat{\mu}_i, \quad (2)$$

where $\hat{V}_i(\hat{x}, \hat{z})$ are the velocity component in the \hat{y} direction and $i = 1$ and 2 refer to fluids 1 and 2 , respectively. While \hat{V}_i is a two-dimensional profile in the \hat{y} direction which depends on \hat{x} and \hat{z} , the velocity components in the \hat{x} and \hat{z} directions are assumed zero. The consideration of a 2D velocity profile (instead of 1D) comes from the fact that in general the effects of the walls cannot be neglected for our restricted low-aspect ratio microchannel geometry.

In order to solve the differential equation (2), we rely on the series decomposition (in terms of hyperbolic functions) of the velocity field, which has been used for similar two-layer fluid mechanics problems.^{6,14,25} The common method is to split the velocity into two terms, $\hat{V}_i(\hat{x}, \hat{z}) = \hat{V}_i^I(\hat{z}) + \hat{V}_i^{II}(\hat{x}, \hat{z})$. The first term is the unperturbed velocity far away from the interface while the second term is expected to vanish far away from the interface and it satisfies Laplace equation $\nabla^2 \hat{V}_i^{II}(\hat{x}, \hat{z}) = 0$. Using the no-slip boundary conditions at the upper and lower walls, the first term can be simply obtained as

$$\hat{V}_i^I(\hat{z}) = \frac{\hat{e}^2 f}{8\hat{\mu}_i} \left[1 - \left(\frac{2\hat{z}}{\hat{e}} \right)^2 \right]. \quad (3)$$

Therefore, the velocity profiles can be expressed analytically as a sum of hyperbolic functions:

$$V_i(x, z) = \frac{f}{8m_i} \left(1 - (2z)^2 + \sum_{n=1}^{\infty} \frac{32(-1)^n}{\Pi^3} \times [\alpha_{i,n} \sinh \Pi x + \beta_{i,n} \cosh \Pi x] \cos \Pi z \right), \quad (4)$$

where $\Pi = (2n - 1)\pi$, $m_1 = m = \hat{\mu}_1/\hat{\mu}_2$ and $m_2 = 1$. Only a few terms of the series are sufficient to obtain reasonable convergence. We have made Equation (4) dimensionless using the channel height \hat{e} as length scale and the mean imposed velocity \hat{V}_0 as velocity scale. Pressure and stresses are made dimensionless with $\hat{\mu}_2 \hat{V}_0 / \hat{e}$. Each mode Π involves two constants for each fluid, i.e., $\alpha_{i,n}$ and $\beta_{i,n}$, which are found through applying the appropriate boundary conditions, i.e., the no-slip boundary conditions at a side wall of the microchannel, the continuity of velocity and tractions at the interface, and the symmetry of the velocity profiles in the middle of the channel (at $y = (H - 2h)/2$). Therefore, the constants can be found as

$$\alpha_{i,n} = \frac{(-1 + \cosh \Pi h - m \cosh \Pi h) \sinh \Pi \mathbf{H}}{m \cosh \Pi h \cosh \Pi \mathbf{H} + \sinh \Pi h \sinh \Pi \mathbf{H}}, \quad (5)$$

$$\beta_{1,n} = \frac{\sinh(\Pi h) \sinh(\Pi \mathbf{H})(1 - m) + m \cosh(\Pi \mathbf{H})}{m \cosh(\Pi h) \cosh(\Pi \mathbf{H}) + \sinh(\Pi h) \sinh(\Pi \mathbf{H})}, \quad (6)$$

$$\beta_{2,n} = \frac{(1 + (m - 1) \cosh(\Pi h)) \cosh(\Pi \mathbf{H})}{m \cosh(\Pi h) \cosh(\Pi \mathbf{H}) + \sinh(\Pi h) \sinh(\Pi \mathbf{H})}, \quad (7)$$

where $\mathbf{H} = (H - 2h)/2$. We now integrate each velocity profile within the corresponding area to find the fluxes in each layer

$$Q_1 = \frac{f}{8m} \left(\frac{2}{3} h - \sum_{n=1}^{\infty} \frac{64}{\Pi^5} [\alpha_{1,n}(1 - \cosh \Pi h) + \beta_{1,n} \sinh \Pi h] \right), \quad (8)$$

$$Q_2 = \frac{f}{8} \left(\frac{4}{3} \mathbf{H} - \sum_{n=1}^{\infty} \frac{128}{\Pi^5} [\alpha_{2,n}(\cosh \Pi \mathbf{H} - 1) + \beta_{2,n} \sinh \Pi \mathbf{H}] \right). \quad (9)$$

In terms of our experiments, the unknown parameter is the viscosity ratio (m). The procedure to find the viscosity ratio through the model is straight-forward. For given h (i.e., measured experimentally) and m (initial guess), the pressure gradient f can be calculated using the flux constraint, i.e., the flux of the solution must be conserved at all times, i.e., $Q_2 = H$. Then,

using the calculated f , the flux of the biofilm layer (Q_1) is calculated. Next, the average speed of the biofilm layer is found through $\bar{V}_1 = Q_1/h$.³² The average speed of the biofilm layer is also measured experimentally. Thus, we can simply iterate on m until we find $\bar{V}_1^{\text{Model}} = \bar{V}_1^{\text{Experiment}}$.

V. MODEL RESULTS

Fig. 4 shows the variation of \bar{V}_1 versus m and h , showing that the average speed of the biofilm increases by h (for a fixed m) and also decreases by m (for a fixed h). However, this figure shows that the dependency of the biofilm viscosity on h is not very strong except near the wall or near the middle of the channel. In the [supplementary material](#) document, we compare this figure with a comparable figure from a different model that we developed in our previous work.¹³

Fig. 5(a) shows the normalized velocity contours ($V_i(x, z)$) in each layer for a fixed interface position ($h = 1$) and the aspect ratio of our microchannel (i.e., $H = 5$) for various values of viscosity ratio (with $m \geq 1$). Note that the velocities in the biofilm layer are multiplied by m for visualization (see [supplementary material](#), Fig. S5 for more clarification and an alternative method of visualization). We observe that for $m > 1$, the normalized biofilm velocity profiles are modified and they are more affected in the biofilm layers. It is evident that the less viscous fluid drags the more viscous fluid so that normalized velocities of the biofilm are the largest close to the interface. Differences between the velocity profiles at $m = 10$ and $m = 10^5$ are minor, implying that the dynamics of the flow becomes nearly independent of the value of the viscosity ratio at very large m .

Fig. 5(b) shows experimental results for the down-stream velocity profile of the wall-adhered biofilm subjected to 0.1 (wt. %) tryptone nutrient solution concentration in the time interval 70–80 h. This time interval was adequately long to follow a sufficient number of biofilm segments. These data were obtained by particle tracking analysis of the velocities of 20 biofilm segments at different \hat{x} -positions between 0 (μm) and 380 (μm) from the microchannel wall, the average width of the biofilm at that time. The average velocity was 7 ($\mu\text{m}/\text{h}$), which compares well with the measured velocity of 6.5 ($\mu\text{m}/\text{h}$) for this sample at the same time in Fig. 2. The model results using the formulation discussed earlier are superimposed on the data. The results are in general agreement with the prediction and the differences, particularly far from the liquid/biofilm interface, are reasonable considering the coarseness of the measurement. However, larger discrepancies exist close to the interface. A number of factors and their combinations could be responsible for this. Some examples could include higher structural heterogeneity that could weaken the biofilm self-adhesion near the edge (see the [supplementary material](#) for a discussion about this), non-homogeneities in the biofilm viscosity throughout the layer, or

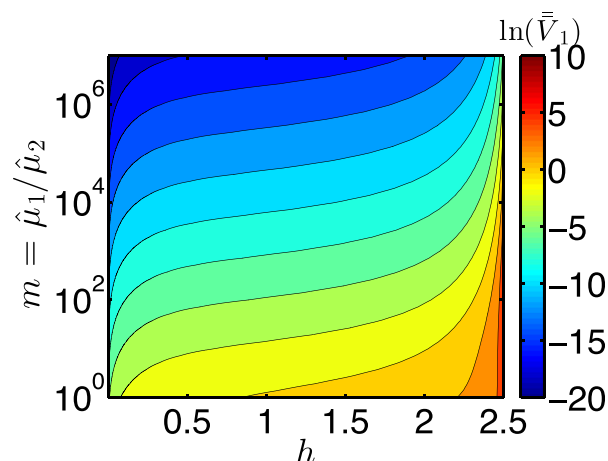


FIG. 4. Contours of $\ln(\bar{V}_1)$ versus m and h for $H = 5$. The color bars represent the values of $\ln(\bar{V}_1)$.

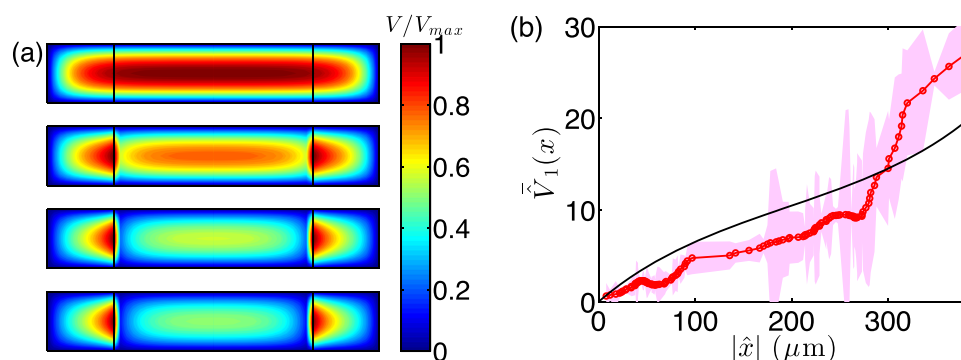


FIG. 5. (a) Normalized velocity contours within the channel cross section in each layer for $h = 1$ and $H = 5$. The velocities in the biofilm layer are multiplied by m for visualization. The color bars show the normalized velocity values. In each sub-figure, the vertical axis shows $-1/2 \leq z \leq 1/2$ and the horizontal axis shows $-1 \leq x \leq 4$. From top to bottom $m = 1, 2, 10, 10^5$, respectively. The vertical dark lines show the position of the interfaces. (b) Velocity profiles (averaged over the thickness of the channel) from experiments and the model velocity profile (averaged depth-wise) for wall-adhered biofilm by experiment (red circles) and the output from the model (black line). Experimental values were obtained from particle tracking at all \hat{x} -coordinates inside the biofilm between the times $\hat{t} = 70$ and $\hat{t} = 80$ h after inoculation under a modified LB nutrient solution containing 0.1 (wt. %) tryptone concentration with flow rate 0.1 (ml/h). The model results are produced through Equation (4) and using the biofilm viscosity from Fig. 6(a) at $\hat{t} = 70$ h for $\hat{h} = 380$ (μm).

differences in bacterial population profiles, which are exacerbated in laminar flows.³⁷ As a next step, to improve the model and shed more light on the spatial variations in mechanical properties near the biofilm surface interface, it may be possible to include viscosity non-homogeneities into our model.

Fig. 6(a) shows the prediction of the (effective) viscosity of the biofilm increasing with time. To obtain this figure, the experimental data from Figs. 2(a) and 2(b) have been used as inputs to the model.

VI. DISCUSSION

The approach to modeling biofilm viscosity in this work resulted in two principle experimental differences compared to other approaches in the literature. The first was that it enabled measurements that were largely passive, in the sense that it did not perturb the biofilm beyond the constant laminar flow of the nutrient solution through the microchannel growth cell. To this end, the applied shear force was approximated to be between 5.2×10^{-4} (Pa) for an

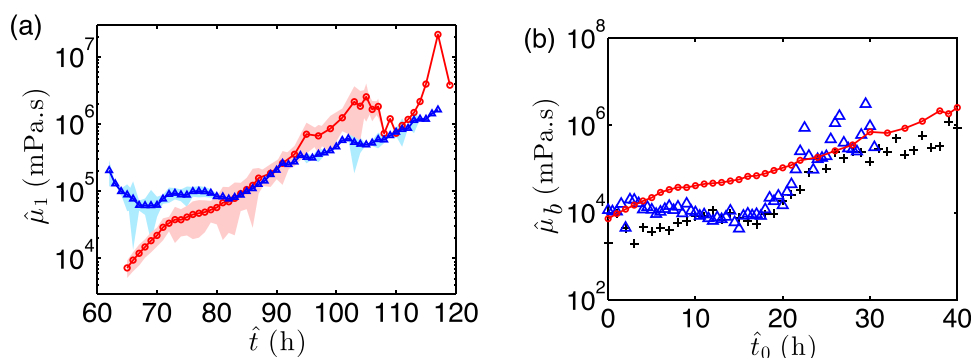


FIG. 6. (a) Viscosity of the biofilm layer ($\hat{\mu}_1$) versus time (\hat{t}) predicted based on the model. Two different nutrient concentrations are shown: 0.02 (wt. %) (solid blue triangles) and 0.1 (wt. %) (red circles). In calculation of the viscosity, shaded error bands were estimated through the accumulation of uncertainty in the measurement of the velocity and the width of the biofilm. (b) A plot of measured viscosity of *Pseudomonas* sp. biofilms ($\hat{\mu}_b$) grown in microfluidic flow cells under 0.1 (wt. %) nutrient concentration versus time after formation (\hat{t}_0) as a result of the experimental and modeling approach used here (red circles) compared to ones developed earlier (+ and open blue triangles).^{13,35} Experimental conditions were nearly identical in all cases, except the flow rates, which were 0.1 (ml/h) in this work compared to 0.2 (ml/h) in the others.

unconstricted microchannel (no biofilm growth) and 8.7×10^{-4} (Pa) for a biofilm with $\hat{w} = 400$ (μm). Second, the measurements were continuous over 5 days with the maximum time resolution of 30 min. This enabled measurements of viscosity throughout the experiment. The results provided by the proof of principle experiment demonstrate the utility of the technique (Fig. 6(a)). The time resolution of the technique revealed initial differences of over an order of magnitude in viscosities of biofilms grown under different nutrient concentrations. Good time resolution also revealed a subsequent normalization of viscosities between the two samples, which was likely related to the time required for bacteria to regulate biochemical conditions to realize viscous properties suited to the nearly similar shear environments in both cases. With the exception of the first 20 h for growth under 0.02 (wt. %), a continuous thickening led to increased viscosities between 10 (Pa s) to over 1000 (Pa s). Since it is unlikely that the slight changes to shear stress could cause such a dramatic shear thickening, we assume that chemical and structural changes related to aging were instead responsible. Consulting the literature, viscosity measurements made on *P. aeruginosa*, which has been shown to share mechanical and chemical similarities to *Pseudomonas fluorescens*, have been measured in the range of 10–10⁶ (Pa s).^{22,48} Thus, our results show overlap with literature reports, but are on the lower end. Longer duration experiments should be conducted to determine how our measurements, which are still increasing after 120 (h), compare to the higher end of viscosity values reported in the literature. We acknowledge the assumption in the repeatability of the proof of principle data sets, which should be validated in new work focusing on experimental measurements. Here, we validate the general trends of the data based on a comparison to recently published results from a second distinct approach. Fig. 6(b) shows a comparison between data acquired in this study with results from the different experiments, in which the same chemical conditions and biofilm forming bacteria were used.³⁵ As seen from Fig. 6(b), results show similar trends in terms of the absolute values of viscosity and the general thickening in time. The main difference in the data set generated by the current approach is the lack of a marked onset of a rapid thickening phase in which the biofilm viscosity increase by over an order of magnitude in less than 10 h. Readers are referred to the [supplementary material](#) document for a more detailed comparison of the two techniques and their results.

The approach presented here also opens the way for similar measurements under different imposed shear stresses to more accurately probe the interplay relationship between it and viscosity. Further experimentation using this technique can hopefully lead to a better understanding of the origins of the vast differences in measured biofilm viscosities. Measurements on different biofilm strains will also be important to demonstrate wider applicability of the technique.

Next, moving beyond the proof of principle experiments in this paper, we discuss how to optimize the approach for future work. As seen from Table II, the microscope system should be taken into account in relation to the limits in measurement of biofilm velocity, which impact calculated viscosity. As discussed in more detail in the [supplementary material](#), the minimum resolvable velocity is a function of the resolution of the microscope system in the x, y focal plane ($\hat{\mathbf{R}}_{x,y}$) and the time interval between frames. In the current work, an objective of 2× was used and image frames were analysed every 2 h under highly viscous conditions (slow biofilm velocities). The experimentally determined minimum observable velocity was approximately 1.6 ($\mu\text{m}/$

TABLE II. Experimentally imposed confidence limits on velocity measurements based on numerical apertures and field of views from the experimental system used in the current study.

| Objective zoom | $\bar{\bar{V}}_{1,\min} (\mu\text{m}/\text{h})$ | $\bar{\bar{V}}_{1,\max} (\mu\text{m}/\text{h})$ |
|----------------|---|---|
| 2 | 1.6 | 8000 |
| 4 | 1.5 | 4000 |
| 10 | 1.2 | 1600 |
| 20 | 0.9 | 800 |
| 40 | 0.8 | 400 |
| 60 | 0.7 | 267 |

h). Consulting Fig. 2(b), we can place high and low confidence in viscosity measurements before and after nearly $\hat{t} = 90$ (h), respectively. We note from Fig. 6(a) that this is approximately the time when viscosity values in the 0.1 (wt. %) nutrient solution cease to increase monotonically. High magnification objectives can improve the lower limit on measured velocities, albeit at the expense of field of view and ultimately number of measurements for statistical purposes. The smaller field of view would also reduce the maximum limit on biofilm velocity; however, even at high magnification, the upper limit is already far higher than the fastest speed measured here. This is discussed in more detail in the [supplementary material](#). Alternatively, instead of using higher resolution microscopy to observe subtle movements of biofilms, higher viscosity nutrient solutions (e.g., containing glycerol) could be used to encourage faster flow of the biofilm. A lower aspect ratio channel could encourage biofilm growth in the corners earlier by lowering the vertical distance that the biofilm had to extend to contact both surfaces.

In addition to experimental improvements to get the best results from the existing model, there are some avenues to optimize the model itself. For example, this could be achieved by incorporating viscoelastic properties of biofilms perhaps using a viscoelastic constitutive equation, to be accompanied by appropriate experiments. Finally, going beyond biofilm applications, the presented model can be used for a broad range of fluid dynamics applications, with added particles for visualization, which could complement other microfluidic approaches to rheometry.^{49,59}

VII. CONCLUSIONS

In this work, we present a semi-analytical fluid flow model that calculates time-varying biofilm viscosities, based on time-lapse video microscopy. Low flow rates through low-aspect ratio microfluidic channels supported the growth of side-wall adhered biofilms. This configuration enabled optical microscope measurements of the input parameters to the model, namely, average biofilm thickness at the vertical side-wall and its average velocity in response to the imposed nutrient flow. Unlike in previous work, all measurements were direct and no estimations were required.³⁵ Using an analytical relation that is developed based on classical fluid mechanics, the model then calculates the value of viscosity for a given width and average velocity of the biofilm layer. We used this approach to measure viscosities from biofilms grown under different tryptone concentrations in modified LB nutrients solutions. The results showed that in the first 50 h of growth, viscosities increased by over 2 orders of magnitude. Initial differences in biofilm viscosities under different nutrient concentrations, vanished after nearly one day, after which thickening occurred with approximately the same rate in both samples. The range of values obtained here fall in the lower end of viscosities reported in the literature. Future tests are required to determine if older biofilms will attain viscosities at the higher end after experimental times that extend longer than tested here. In addition to the role of aging, the technique also opens up the ability to probe the role of applied shear stress. We hope that this new methodology can contribute to impressive work from contributors over the last 25 years. Following the development of the model, experimental procedure, and its preliminary application to a single biofilm strain, next steps include measurements on a wider variety of biofilms and growth conditions.

SUPPLEMENTARY MATERIAL

See [supplementary material](#) for detailed descriptions on growth kinetics and biofilm heterogeneity, velocity tracking, nutrient solution viscosity, measuring width of biofilms at the side-walls, comparison with previous studies, clarification on Fig. 5(a) of the main paper and shear stress distribution.

ACKNOWLEDGMENTS

The authors thank the support through Discovery Grant of Natural Sciences and Engineering Research Council of Canada (NSERC) (Grant Nos. CG109154 and CG106382) and the support by Canada Foundation for Innovation (CFI) (Grant No. GF105094). We also thank Professor D.

Rodrigue from the Chemical Engineering Department for providing access to the rheometer and F. Paquet-Mercier for preparing nutrient solution samples for rheometry.

S.M.T. and J.G. conceived the project. M.P.G. conducted biofilm growth and imaging experiments. A.E. performed rheological measurements. M.P.Z. provided help with the experiments. J.G. analysed the experimental data. SMT developed the mathematical model. J.G. and S.M.T. wrote the manuscript.

- ¹P. Barai, A. Kumar, and P. P. Mukherjee, "Mesoscale elucidation of biofilm shear behavior," preprint [arXiv:1509.03926](https://arxiv.org/abs/1509.03926) (2015).
- ²E. Bester, G. Wolfaardt, L. Joubert, K. Garny, and S. Saftic, "Planktonic-cell yield of a pseudomonad biofilm," *Appl. Environ. Microbiol.* **71**(12), 7792–7798 (2005).
- ³E. Bester, G. M. Wolfaardt, N. B. Aznavah, and J. Greener, "Biofilms' role in planktonic cell proliferation," *Int. J. Mol. Sci.* **14**(11), 21965–21982 (2013).
- ⁴N. Billings, A. Birjiniuk, T. S. Samad, P. S. Doyle, and K. Ribbeck, "Material properties of biofilms—A review of methods for understanding permeability and mechanics," *Rep. Prog. Phys.* **78**(3), 036601 (2015).
- ⁵M. Cancela, E. Alvarez, and R. Maceiras, "Effects of temperature and concentration on carboxymethylcellulose with sucrose rheology," *J. Food Eng.* **71**(4), 419–424 (2005).
- ⁶M. Charles and L. Lilleleht, "Co-current stratified laminar flow of two immiscible liquids in a rectangular conduit," *Can. J. Chem. Eng.* **43**(3), 110–116 (1965).
- ⁷F. C. Cheong, S. Duarte, S.-H. Lee, and D. G. Grier, "Holographic microrheology of polysaccharides from *Streptococcus mutans* biofilms," *Rheol. Acta* **48**(1), 109–115 (2009).
- ⁸S. C. Chew, B. Kundukad, T. Seviour, J. R. van der Maarel, L. Yang, S. A. Rice, P. Doyle, and S. Kjelleberg, "Dynamic remodeling of microbial biofilms by functionally distinct exopolysaccharides," *MBio* **5**(4), e01536 (2014).
- ⁹S. Das and A. Kumar, "Formation and post-formation dynamics of bacterial biofilm streamers as highly viscous liquid jets," *Sci. Rep.* **4**, 7126 (2014).
- ¹⁰Y. Ding, N. Peng, Y. Du, L. Ji, and B. Cao, "Disruption of putrescine biosynthesis in *Shewanella oneidensis* enhances biofilm cohesiveness and performance in *cr* (vi) immobilization," *Appl. Environ. Microbiol.* **80**(4), 1498–1506 (2014).
- ¹¹B. Dunsmore, A. Jacobsen, L. Hall-Stoodley, C. Bass, H. Lappin-Scott, and P. Stoodley, "The influence of fluid shear on the structure and material properties of sulphate-reducing bacterial biofilms," *J. Ind. Microbiol. Biotechnol.* **29**(6), 347–353 (2002).
- ¹²H. J. Eberl and R. Sudarsan, "Exposure of biofilms to slow flow fields: The convective contribution to growth and disinfection," *J. Theor. Biol.* **253**(4), 788–807 (2008).
- ¹³M. P. Gashti, J. Bellavance, O. Kroukamp, G. Wolfaardt, S. M. Taghavi, and J. Greener, "Live-streaming: Time-lapse video evidence of novel streamer formation mechanism and varying viscosity," *Biomicrofluidics* **9**(4), 041101 (2015).
- ¹⁴P. Gondret, N. Rakotomalala, M. Rabaud, D. Salin, and P. Watzky, "Viscous parallel flows in finite aspect ratio Hele-Shaw cell: Analytical and numerical results," *Phys. Fluids* **9**(6), 1841–1843 (1997).
- ¹⁵G. W. Hanlon, S. P. Denyer, C. J. Olliff, and L. J. Ibrahim, "Reduction in exopolysaccharide viscosity as an aid to bacteriophage penetration through *Pseudomonas aeruginosa* biofilms," *Appl. Environ. Microbiol.* **67**(6), 2746–2753 (2001).
- ¹⁶A. Karimi, D. Karig, A. Kumar, and A. Ardekani, "Interplay of physical mechanisms and biofilm processes: Review of microfluidic methods," *Lab Chip* **15**(1), 23–42 (2015).
- ¹⁷J. Kim, H.-S. Kim, S. Han, J.-Y. Lee, J.-E. Oh, S. Chung, and H.-D. Park, "Hydrodynamic effects on bacterial biofilm development in a microfluidic environment," *Lab Chip* **13**(10), 1846–1849 (2013).
- ¹⁸J. Kim, H.-D. Park, and S. Chung, "Microfluidic approaches to bacterial biofilm formation," *Molecules* **17**(8), 9818–9834 (2012).
- ¹⁹I. Klapper, C. Rupp, R. Cargo, B. Purvedorj, and P. Stoodley, "Viscoelastic fluid description of bacterial biofilm material properties," *Biotechnol. Bioeng.* **80**(3), 289–296 (2002).
- ²⁰V. Körstgens, H.-C. Flemming, J. Wingender, and W. Borchard, "Influence of calcium ions on the mechanical properties of a model biofilm of mucoid *Pseudomonas aeruginosa*," *Water Sci. Tech.* **43**(6), 49–57 (2001).
- ²¹O. Kroukamp, R. G. Dumitrache, and G. M. Wolfaardt, "Pronounced effect of the nature of the inoculum on biofilm development in flow systems," *Appl. Environ. Microbiol.* **76**(18), 6025–6031 (2010).
- ²²P. C. Lau, J. R. Dutcher, T. J. Beveridge, and J. S. Lam, "Absolute quantitation of bacterial biofilm adhesion and viscoelasticity by microbead force spectroscopy," *Biophys. J.* **96**(7), 2935–2948 (2009).
- ²³O. Lieleg, M. Caldara, R. Baumgärtel, and K. Ribbeck, "Mechanical robustness of *Pseudomonas aeruginosa* biofilms," *Soft Matter* **7**(7), 3307–3314 (2011).
- ²⁴J. Liu, M. Gardel, K. Kroy, E. Frey, B. D. Hoffman, J. C. Crocker, A. Bausch, and D. Weitz, "Microrheology probes length scale dependent rheology," *Phys. Rev. Lett.* **96**(11), 118104 (2006).
- ²⁵J. Martin, N. Rakotomalala, L. Talon, and D. Salin, "Viscous lock-exchange in rectangular channels," *J. Fluid Mech.* **673**, 132–146 (2011).
- ²⁶J. Mathias and P. Stoodley, "Applying the digital image correlation method to estimate the mechanical properties of bacterial biofilms subjected to a wall shear stress," *Biofouling* **25**(8), 695–703 (2009).
- ²⁷M. G. Mazza, "The physics of biofilms—An introduction," *J. Phys. D: Appl. Phys.* **49**(20), 203001–203024 (2016).
- ²⁸E. Meijering, O. Dzyubachyk, and I. T. Smal, "Methods for cell and particle tracking," *Methods Enzymol.* **504**(9), 183–200 (2012).
- ²⁹T. Merkel, V. Bondar, K. Nagai, B. Freeman, and I. Pinnau, "Gas sorption, diffusion, and permeation in poly(dimethylsiloxane)," *J. Polym. Sci. Part B Polym. Phys.* **38**(3), 415–434 (2000).
- ³⁰S. Neethirajan, D. Karig, A. Kumar, P. P. Mukherjee, S. T. Retterer, and M. J. Doktycz, "Biofilms in microfluidic devices," in *Encyclopedia of Nanotechnology* (Springer, 2012), pp. 213–219.

- ³¹In this paper, we adopt the convention of denoting dimensional quantities with the $\hat{\cdot}$ symbol and dimensionless quantities without.
- ³²Note that the parameters with a single overbar sign are averaged over \hat{z} and the parameters with two overbar signs are averaged over \hat{x} and \hat{z} .
- ³³J.-C. Ochoa, C. Coufort, R. Escudié, A. Liné, and E. Paul, "Influence of non-uniform distribution of shear stress on aerobic biofilms," *Chem. Eng. Sci.* **62**(14), 3672–3684 (2007).
- ³⁴R. Pamies, R. R. Schmidt, M. d., C. L. Martínez, and J. G. de la Torre, "The influence of mono and divalent cations on dilute and non-dilute aqueous solutions of sodium alginates," *Carbohydr. Polym.* **80**(1), 248–253 (2010).
- ³⁵F. Paquet-Mercier, M. P. Gashti, J. Bellavance, S. M. Taghavi, and J. Greener, "Through thick and thin: A microfluidic approach for continuous measurements of biofilm viscosity," *Lab Chip* (published online, 2016).
- ³⁶L. Pavlovsky, J. G. Younger, and M. J. Solomon, "In situ rheology of staphylococcus epidermidis bacterial biofilms," *Soft Matter* **9**(1), 122–131 (2013).
- ³⁷M. O. Pereira, M. Kuehn, S. Wuertz, T. Neu, and L. F. Melo, "Effect of flow regime on the architecture of a *Pseudomonas fluorescens* biofilm," *Biotechnol. Bioeng.* **78**(2), 164–171 (2002).
- ³⁸C. Picioreanu, M. C. Van Loosdrecht, and J. J. T. Heijnen, "Mathematical modeling of biofilm structure with a hybrid differential-discrete cellular automaton approach," *Biotechnol. Bioeng.* **58**(1), 101–116 (1998).
- ³⁹C. Picioreanu, M. C. Van Loosdrecht, and J. J. T. Heijnen, "Effect of diffusive and convective substrate transport on biofilm structure formation: A two-dimensional modeling study," *Biotechnol. Bioeng.* **69**(5), 504–515 (2000).
- ⁴⁰C. Picioreanu, M. C. Van Loosdrecht, and J. J. t. Heijnen, "Two-dimensional model of biofilm detachment caused by internal stress from liquid flow," *Biotechnol. Bioeng.* **72**(2), 205–218 (2001).
- ⁴¹L. Pitsyn, G. Horneck, O. Komova, S. Kozubek, E. Krasavin, M. Bonev, and P. Rettberg, "A biosensor for environmental genotoxin screening based on an *soxS* lux assay in recombinant *Escherichia coli* cells," *Appl. Environ. Microbiol.* **63**(11), 4377–4384 (1997).
- ⁴²L. D. Renner and D. B. Weibel, "Physicochemical regulation of biofilm formation," *MRS Bull.* **36**(05), 347–355 (2011).
- ⁴³B. E. Rittman, "The effect of shear stress on biofilm loss rate," *Biotechnol. Bioeng.* **24**(2), 501–506 (1982).
- ⁴⁴S. Rogers, C. Van Der Walle, and T. Waigh, "Microrheology of bacterial biofilms in vitro: *Staphylococcus aureus* and *Pseudomonas aeruginosa*," *Langmuir* **24**(23), 13549–13555 (2008).
- ⁴⁵C. J. Rupp, C. A. Fux, and P. Stoodley, "Viscoelasticity of *Staphylococcus aureus* biofilms in response to fluid shear allows resistance to detachment and facilitates rolling migration," *Appl. Environ. Microbiol.* **71**(4), 2175–2178 (2005).
- ⁴⁶R. Rusconi, N. Lecuyer, N. Autrusson, L. Guglielmini, and H. A. Stone, "Secondary flow as a mechanism for the formation of biofilm streamers," *Biophys. J.* **100**(6), 1392–1399 (2011).
- ⁴⁷C. A. Schneider, W. S. Rasband, and K. W. T. Eliceiri, "NIH image to ImageJ: 25 years of image analysis," *Nat. Methods* **9**(7), 671–675 (2012).
- ⁴⁸T. Shaw, M. Winston, C. Rupp, I. Klapper, and P. Stoodley, "Commonality of elastic relaxation times in biofilms," *Phys. Rev. Lett.* **93**(9), 098102 (2004).
- ⁴⁹D. E. Solomon and S. A. Vanapalli, "Multiplexed microfluidic viscometer for high-throughput complex fluid rheology," *Microfluid. Nanofluid.* **16**(4), 677–690 (2014).
- ⁵⁰K. J. Sreeram, H. Y. Shrivastava, and B. U. Nair, "Studies on the nature of interaction of iron (iii) with alginates," *Biochim. Biophys. Acta* **1670**(2), 121–125 (2004).
- ⁵¹P. Stoodley, R. Cargo, C. Rupp, S. Wilson, and I. Klapper, "Biofilm material properties as related to shear-induced deformation and detachment phenomena," *J. Ind. Microbiol. Biotechnol.* **29**(6), 361–367 (2002).
- ⁵²P. Stoodley, Z. Lewandowski, J. D. Boyle, and H. M. T. Lappin-Scott, "Structural deformation of bacterial biofilms caused by short-term fluctuations in fluid shear: An in situ investigation of biofilm rheology," *Biotechnol. Bioeng.* **65**(1), 83–92 (1999).
- ⁵³T. K. Van Dyk, W. R. Majarian, K. B. Konstantinov, R. M. Young, P. S. Dhurjati, and R. A. Larossa, "Rapid and sensitive pollutant detection by induction of heat shock gene-bioluminescence gene fusions," *Appl. Environ. Microbiol.* **60**(5), 1414–1420 (1994).
- ⁵⁴A. Vinogradov, M. Winston, C. Rupp, and P. Stoodley, "Rheology of biofilms formed from the dental plaque pathogen *Streptococcus mutans*," *Biofilms* **1**(01), 49–56 (2004).
- ⁵⁵Q. Wang and T. Zhang, "Review of mathematical models for biofilms," *Solid State Commun.* **150**(21), 1009–1022 (2010).
- ⁵⁶J. P. Ward and J. R. King, "Thin-film modelling of biofilm growth and quorum sensing," *J. Eng. Math.* **73**(1), 71–92 (2012).
- ⁵⁷A. Wileman, A. Ozkan, and H. Berberoglu, "Rheological properties of algae slurries for minimizing harvesting energy requirements in biofuel production," *Bioresour. Technol.* **104**, 432–439 (2012).
- ⁵⁸G. Wolfaardt, M. Hendry, T. Birkham, A. Bressel, M. Gardner, A. Sousa, D. Korber, and M. Pilaski, "Microbial response to environmental gradients in a ceramic-based diffusion system," *Biotechnol. Bioeng.* **100**(1), 141–149 (2008).
- ⁵⁹J. Zilz, C. Schäfer, C. Wagner, R. J. Poole, M. A. Alves, and A. Lindner, "Serpentine channels: Micro-rheometers for fluid relaxation times," *Lab Chip* **14**(2), 351–358 (2014).